Physics of Fluids

RESEARCH ARTICLE | JULY 05 2023

Investigation of particle size impact on dense particulate flows in a vertical pipe

Ren Wan-Long (任万龙) ; Zhang Xu-Hui (张旭辉) ; Zhang Yan (张岩) ; Li Peng (李鹏) ; Lu Xiao-Bing (鲁晓兵)

Physics of Fluids 35, 073302 (2023)
https://doi.org/10.1063/5.0157609

Physics of Fluids ARTICLE pubs.aip.org/aip/pof

Investigation of particle size impact on dense particulate flows in a vertical pipe

Cite as: Phys. Fluids **35**, 073302 (2023); doi: 10.1063/5.0157609
Submitted: 9 May 2023 · Accepted: 13 June 2023 ·
Published Online: 5 July 2023

Wan-Long Ren (任万龙),[1,2] Xu-Hui Zhang (张旭辉),[1,2] Yan Zhang (张岩),[1,a)] Peng Li (李鹏),[1] and Xiao-Bing Lu (鲁晓兵)[1,2]

AFFILIATIONS

[1]Institute of Mechanics, Chinese Academy of Sciences, Beijing 100190, China
[2]School of Engineering Science, University of Chinese Academy of Sciences, Beijing 100049, China

[a)]Author to whom correspondence should be addressed: zhangyan162@imech.ac.cn

ABSTRACT

In this work, a semi-resolved computational fluid dynamics-discrete element method is employed to study the effects of fluid–particle and particle–particle/wall interactions on particle mixing and segregation behaviors and particle dynamics with different particle sizes in a vertical pipe. There are two species of particles with the same density in the vertical pipe: $d_1 = 10$ (species 1) and $d_2 = 2$–7 mm (species 2), and species 2 contains both fine and coarse particles. The Stokes number St_p is introduced to characterize the effects of different particle sizes on particle dynamics. First, the particle mixing and segregation behaviors with different size ratios are qualitatively analyzed. By comparing with smaller size ratios, obvious granular plugs and stronger contact force networks occur at larger size ratios. Second, after the segregation of species 1 and 2, the differences in dynamic characteristics between fine and coarse particles are explored. The normalized autocorrelation length scale, which is the ratio of propagation length of particle velocity fluctuations and particle diameter, is significantly different from fine to coarse particles. One notable feature is that two different flow regimes are found through the radial distribution function. Furthermore, the hydrodynamic stress and collision stress are defined to study the mechanism for the differences between fine and coarse particles. The results imply that the reason for the differences is that the collision effects go beyond the hydrodynamic effects with the increase in the Stokes number.

I. INTRODUCTION

Fluidized beds have been widely applied to many industrial processes, such as chemical synthesis, mining industries, and wastewater treatment, all attributed to their sufficient solid–liquid contact, good heat and mass transfer, low operation cost, and friendliness to the environment.[1,2] The typical fluidized beds using solid particles of the same size and density can exhibit a homogeneous fluidization phenomenon, and they have been well predicted by the classical equation proposed by Richardson and Zaki.[3] However, a wide size distribution for particles is extensively practiced in current industrial operations. By comparing with mono-disperse particles, fluidized beds with a wide size distribution will exhibit different particle mixing and segregation behaviors.[4] In addition, the dynamics characteristics of fluidized beds are intrinsically complicated due to particle–fluid and particle–particle/wall interactions, especially if the solid particles have a wide size distribution.[5] Moreover, the fluidized beds with a wide size distribution may exhibit particle aggregation phenomena, such as unsafe behaviors-plugs and pipe blockage.[6] Therefore, it is very significant to understand the effects of different particle sizes on particulate flows, such as particle mixing and segregation behaviors, and then provide recommendations for optimizing fluidization behaviors.

Over the past decades, many researchers have conducted a large number of experimental and numerical studies to understand the characteristics and mechanisms of particle mixing and segregation.[7–9] After extensive research, the segregation modes in fluidized beds could be categorized into three types: no segregation, partial segregation, and complete segregation.[8,9] Most researchers chose binary fluidized beds with different particle size ratios or densities to study the particle mixing and segregation.[10–12] For example, the layer inversion phenomenon can often be observed in binary fluidized beds where the larger particles have a smaller density than smaller particles.[5] Moreover, the layer inversion is considered a collection of three types of segregation, depending on the relationship between the inlet fluid velocity and the minimum fluidization velocity.[4] When the inlet fluid velocity is slightly greater than the minimum fluidization velocity, layer inversion can happen. Table I summarizes particle and pipe information in binary fluidized beds. From these studies, it is obvious to be seen that the ratio of particle size to pipe diameter is generally small, which may be

TABLE I. The typical experimental and numerical simulation data of binary fluidized beds.

Authors	D (mm)	d_1 (mm)	d_2 (mm)	d_1/D	d_2/D
Xie *et al.*[4]	50	4	1	0.08	0.02
Epstein and LeClair[5]	50.8	3.15	2.05	0.06	0.04
Di Renzo *et al.*[8]	38.2	1.08	0.65	0.0282	0.0170
Moritomi *et al.*[10]	50	0.775	0.163	0.016	0.003
Zhou and Yu[18]	150	0.78	0.19	0.005	0.001
Molaei *et al.*[19]	10	0.778	0.193	0.078	0.019

because the particle size needs to be as small as possible to increase the solid–fluid contact in gas–solid fluidized beds.[13] However, in liquid-solid fluidized beds, especially in mining industries, the particle size is coarse.[14] Coarse particles refer to particles with a ratio of particle size to pipe diameter not less than about 0.1.[15,16] For binary fluidized beds with coarse particles, Cúñez and Franklin[17] investigated the layer inversion with two different solid species in a vertical pipe through experimental and numerical methods. The pipe diameter was $D = 25.4$ mm, and two different solid species were as follows: $d_1 = 6$ mm and $\rho_1 = 3690\,\mathrm{kg/m^3}$, $d_2 = 4.8$ mm and $\rho_2 = 2760\,\mathrm{kg/m^3}$. The d_p/D were 0.236 and 0.189, respectively. Finally, they qualitatively analyzed the layer inversion and gave the characteristic time for layer inversion. Ren *et al.*[14] studied the characteristics and formation mechanisms of layer inversion in binary fluidized beds by changing fluid velocity. The fluidized bed was formed in a 50 mm-ID cylindrical pipe and composed of two species of coarse particles with the same density: $d_1 = 10$, $d_2 = 6$ mm. The d_p/D was 0.2 and 0.12, respectively. They found the relative magnitude of fluid–solid interaction force, and the net gravity was the main reason for layer inversion. It is worth noting that there were only two particle sizes in their binary fluidized beds. However, in realistic industry operations, particles have a wide size distribution. Hence, it is necessary to study particle mixing and segregation behaviors with both coarse particles and a wide size distribution.

By comparing with fine particles (about $d_p/D < 0.1$), there is no doubt that the dynamics with coarse particles are complicated.[20,21] In the past decade, some papers have reported some obvious findings at about $d_p/D \geq 0.1$ in a vertical pipe. When the ratio of particles to pipe diameter was between 0.1 and 0.001 in the experiments, Duru and Guazzelli[20] found that transverse waves, blobs, and bubbles would appear. While particle size was larger than about 0.1 times the pipe diameter, the fluidized beds may become jammed due to the formation of upward arches of particle flow, which could cause the disappearance of fluctuations.[21] Van Wijk *et al.*[16] conducted experiments on hydraulic transport in a vertical pipe. They found that when the ratio of particle size to pipe diameter d_p/D was about 0.1, the flow was instability and detrimental to the transport process. When $d_p/D > 0.2$, Cúñez and Franklin[15] studied the dynamic characteristics of the fluidized beds using experiments and computational fluid dynamics-discrete element methods (CFD-DEM). They qualitatively evidenced the effect of strong constraints of wall on bed dynamics through a dense network of contact forces from the center of the pipe to the pipe wall. In addition, Cúñez *et al.*[22] also explored bed dynamics with duos and trios of bonded coarse particles. They found the fluidized beds would exhibit obvious instability due to wall constraints, and the jamming may occur suddenly for bonded coarse particles depending on the grain type. Zhang *et al.*[23] investigated the characteristics of hydraulic conveying with dense coarse particles in a vertical pipe, and their results showed various unstable flow patterns, such as dilute-dense and plug flow patterns. Although they discover some significant changes when d_p/D is not less than about 0.1, quantitative dynamics characteristics between fine and coarse particles and the mechanism are still unclear. The relevant research is rarely reported. Some papers defined coarse particles without considering the pipe diameter.[24,25] Therefore, it is also significant to quantitatively explore the differences in dynamics of coarse and fine particles and reveal the mechanism for the differences.

Although experiments are very important means to study the particle dynamics in fluidized beds, it is difficult to obtain information about individual particles over time. Detailed information about particles, such as particle/fluid distribution and particle–fluid interaction forces, can be easily obtained from the numerical simulation. The information can be further used to analyze particle mixing and segregation behaviors with different size ratios as well as the dynamic characteristics.[14] Thus, in this paper, we will study the effects of the particle sizes on particulate flows in fluidized beds using the Eulerian–Lagrangian (E–L) methods.[26,27] For the E–L methods, the fluid field is solved in Eulerian meshes, and the motion information of individual particles is obtained in a Lagrangian way.[28] It can be classified into two subcategories: (1) resolved computational fluid dynamics-discrete element methods (CFD-DEM) and[29–31] (2) unresolved CFD-DEM.[32–34] In resolved CFD-DEM, particle–fluid and particle–particle/wall interaction forces can be fully resolved without using any empirical force models, which also brings a large amount of computational cost and is not suitable for a large amount of particles.[35] To achieve high computational accuracy, the resolved CFD-DEM usually requires the ratio of mesh size to particle size less than 0.1.[31] In the unresolved CFD-DEM, fluid–solid interaction forces, such as drag force, are calculated by various empirical equations, and it is not necessary to accurately describe the particle boundary and analyze the flow field around particles. Therefore, it dramatically improves the computational efficiency and the number of particles.[36] To better capture this information, the unresolved CFD-DEM usually requires a mesh size greater than three times the particle diameter.[35] However, when the mesh size of CFD is 0.1–3 times the particle size, the results of both resolved and unresolved CFD-DEM methods are not accurate.[37] Our work has the characteristics of both coarse particles and different size ratios, which leads to the ratio of mesh size to particle size belonging to this range. Thus, an unresolved CFD-DEM that can meet both the number of particles and particle size is required. In our previous work,[38] an optimized unresolved CFD-DEM has been proposed to meet the need, and it is referred to as a semi-resolved CFD-DEM.

The semi-resolved CFD-DEM has been implemented into the open-source code computational fluid dynamics/discrete element method (CFDEM).[39] The fluid field is solved by the open source code Open Field Operation Manipulation (OpenFOAM)[6] while the individual particle information is calculated by the open source code LAMMPS improved for general granular and granular heat transfer simulations (LIGGGHTS),[40] both are linked via the open source code CFDEM. It can greatly improve computational efficiency since particulate flows and flow fields are solved separately.[14]

The aims of this article are to analyze particle mixing and segregation behaviors with different size ratios, then quantitatively study the differences in dynamic characteristics between coarse and fine particles, and reveal the mechanism for the differences.

The paper is organized as follows. In Sec. II, the governing equations of the semi-resolved CFD-DEM are introduced. In Sec. III, the geometric settings and conditions for numerical simulation are given. In Sec. IV, the model is validated. In Sec. V, the results of particle mixing and segregation behaviors and particle dynamics are shown. Finally, the main findings are summarized in Sec. VI.

II. MODEL DESCRIPTION

A. Solid phase

A single particle has translational and rotational motions in a solid–liquid two-phase flow, which is solved based on Newton's second law. The expressions[41] are as follows:

$$m_p \frac{\mathrm{d}\boldsymbol{u}_p}{\mathrm{d}t} = \boldsymbol{f}_{fp} + m_p\boldsymbol{g} + \sum_{i\neq j}^{N_c}\boldsymbol{f}_{c,ij} + \sum_{i}^{N_w}\boldsymbol{f}_{c,iw}, \tag{1}$$

$$I_p \frac{\mathrm{d}\boldsymbol{\omega}_p}{\mathrm{d}t} = \sum_{i\neq j}^{N_c}\boldsymbol{T}_{p,ij} + \sum_{i}^{N_w}\boldsymbol{T}_{p,iw}, \tag{2}$$

where m_p is the mass of the particle; $\boldsymbol{u}_p$ and $\boldsymbol{\omega}_p$ are the translational and angular velocities of the particle i, respectively; and $\boldsymbol{f}_{pf}$ is the fluid-particle interaction force; and it can be expressed by

$$\boldsymbol{f}_{fp,i} = \boldsymbol{f}_{d,i} + \boldsymbol{f}_{\nabla p,i} + \boldsymbol{f}_{\nabla\cdot\boldsymbol{\tau},i} + \boldsymbol{f}_{lift,i} + \boldsymbol{f}_{vm,i}, \tag{3}$$

where $\boldsymbol{f}_{d,i}$ is the drag force; $\boldsymbol{f}_{\nabla\cdot\boldsymbol{\tau},i}$ is the viscous force; $\boldsymbol{f}_{\nabla p,i}$ is the pressure gradient force; $\boldsymbol{f}_{lift,i}$ and $\boldsymbol{f}_{vm,i}$ are the lift force and the virtual mass force, respectively; $\boldsymbol{f}_{c,ij}$ and $\boldsymbol{f}_{c,iw}$ are the collision forces of particle i to particle j and wall w, respectively, $\boldsymbol{T}_{ij}$ is the torque generated by the tangential component of the collision forces between particles i and j; and $\boldsymbol{T}_{iw}$ is the torque generated by the tangential component of the collision forces between particles i and the wall w. The collision forces and torques between particles are the sums of particles i in contact with other $N_c - 1$ particles, and N_c is the number of all particles. The particle–wall collision forces and torques are the sums of N_w particles in contact with the wall. The soft sphere model is used to calculate the particle–particle/wall collision forces.[42,43] The model is expressed as follows:

$$\boldsymbol{f}_{c,ij} = \boldsymbol{f}_{cn,ij} + \boldsymbol{f}_{ct,ij}, \tag{4}$$

$$\boldsymbol{F}_{cn,ij} = \left(k_n\delta_{n,ij}^{\frac{3}{2}} - \eta_n\boldsymbol{u}_{ij}\cdot\boldsymbol{n}_{ij}\right)\boldsymbol{n}_{ij}, \tag{5}$$

$$\boldsymbol{F}_{ct,ij} = \left(k_t\delta_{t,ij} - \eta_t\boldsymbol{u}_{s,ij}\cdot\boldsymbol{t}_{ij}\right)\boldsymbol{t}_{ij}, \tag{6}$$

where n and t represent the normal and tangential directions at the contact point, k and η are the spring coefficient and the damping coefficient, respectively, $\boldsymbol{\delta}$ is the overlap between particle i and particle j, and k and η can be calculated based on the Hertzian model.[6,44]

B. Fluid phase

The fluid phase is described by the volume-averaged incompressible Navier–Stokes (N–S) equations. The pressure and velocity are solved by the mass and momentum equations[45]

$$\frac{(\partial\rho_f\alpha_f)}{\partial t} + \nabla\cdot(\rho_f\alpha_f\boldsymbol{u}_f) = 0, \tag{7}$$

$$\frac{\partial(\rho_f\alpha_f\boldsymbol{u}_f)}{\partial t} + \nabla\cdot(\rho_f\alpha_f\boldsymbol{u}_f\boldsymbol{u}_f) = -\alpha_f\nabla p - \boldsymbol{F}_{pf} + \alpha_f\nabla\cdot\boldsymbol{\tau}_f + \rho_f\alpha_f\boldsymbol{g}, \tag{8}$$

where ∇P is the pressure gradient, $\boldsymbol{u}_f$ is the mean fluid velocity, α_f is the void fraction of the fluid, $\boldsymbol{\tau}_f$ is the stress tensor, $\boldsymbol{g}$ is the acceleration of gravity, and $\boldsymbol{F}_{pf}$ is the volumetric fluid–particle interaction force, and it is computed by

$$\boldsymbol{F}_{pf} = \frac{1}{V_c}\sum_{i=1}^{n}\left(\boldsymbol{f}_{d,i} + \boldsymbol{f}_{lift,i} + \boldsymbol{f}_{vm,i}\right), \tag{9}$$

where V_c is the volume of the CFD cells.

$\boldsymbol{\tau}_f$ is expressed as follows:

$$\boldsymbol{\tau}_f = \nu_f\left(\nabla\boldsymbol{u}_f + \nabla\boldsymbol{u}_f^{\mathrm{T}}\right) - \frac{2}{3}\nu_f\nabla\cdot\boldsymbol{u}_f\boldsymbol{I}, \tag{10}$$

where ν_f is the viscosity coefficient of fluid and $\boldsymbol{I}$ is the unit matrix.

C. Fluid–solid interaction

In the semi-resolved CFD-DEM, the particle–fluid two phases are coupled through void fraction α_f and particle–fluid interaction force $\boldsymbol{f}_{fp,i}$, and CFD cells and particles are linked based on the position of the particles.[38] The drag force, pressure gradient force, Magnus lift force, and virtual force need to be considered in the fluidized beds.[17,23] The drag force between particles and fluid is calculated by the Wen–Yu model,[46]

$$\boldsymbol{F}_{fp} = k_d(\boldsymbol{u}_f - \boldsymbol{u}_p), \tag{11}$$

$$k_d = \begin{cases} \alpha_f < 0.8, & V_p\left(150\dfrac{(1-\alpha_f)}{\alpha_f}\dfrac{\mu_f}{d^2} + 1.75\dfrac{\rho_f|\boldsymbol{u}_f - \boldsymbol{u}_p|}{d}\right), \\ \alpha_f \geq 0.8, & V_p\dfrac{3}{4}C_d\dfrac{\rho_f|\boldsymbol{u}_f - \boldsymbol{u}_p|}{d}\alpha_f^{-2.65}, \end{cases} \tag{12}$$

$$C_d = \begin{cases} Re_{fp} < 1000, & \dfrac{24(1 + 0.15Re0.687)}{Re}, \\ Re_{fp} \geq 1000, & 0.424, \end{cases} \tag{13}$$

$$Re_{fp} = \frac{\rho_f|\boldsymbol{u}_f - \boldsymbol{u}_p|d}{\mu_f}, \tag{14}$$

where V_p is the particle volume, μ_f is the shear viscosity of fluid, C_d is the drag coefficient, and Re_{fp} is the Reynolds number of particle–liquid relative motion.

The pressure gradient[43] is expressed as follows:

$$\boldsymbol{f}_{\nabla p} = -V_p\nabla p, \tag{15}$$

where V_p is the particle volume.

The Magnus lift force[47] is written as follows:

$$\boldsymbol{f}_{lift} = \frac{1}{8}C_L\rho_f\pi{d_p}^2|\boldsymbol{u}_f - \boldsymbol{u}_p|\left[(\boldsymbol{u}_f - \boldsymbol{u}_p)\times\frac{\nabla\times\boldsymbol{u}_f}{|\nabla\times\boldsymbol{u}_f|}\right], \tag{16}$$

where C_L is the lift coefficient, which is calculated by Loth and Dorgan.[47]

The expression of the virtual mass force[45] is

$$f_{vm} = C_{vm} m_p \frac{\rho_f}{\rho_p}\left(u_p \nabla u_f - \frac{du_p}{dt}\right), \tag{17}$$

where C_{vm} is the virtual mass force coefficient, which is typically equal to 0.5.[45]

D. Virtual mass distribution function (VMDF)

There is a solid–liquid two-phase flow in the fluidized beds with coarse particles. The solid particles are solved in the Lagrangian field, and the fluid is solved in the Eulerian field, which are coupled by the void fraction and fluid–particle interaction forces. When the CFD mesh contains multiple particles, the particle void fraction and fluid-particle interaction forces are calculated as follows:

$$\alpha_{\mathrm{p},b} = \sum_{a=1}^{n_b} V_{\mathrm{p},a}/V_{\mathrm{cell},b}, \tag{18}$$

$$\mathbf{f}_{\mathrm{pf},b} = \frac{1}{V_{\mathrm{cell},b}} \sum_{a=1}^{n_b} \mathbf{F}_{\mathrm{pf},a}, \tag{19}$$

where $\alpha_{\mathrm{p},b}$ is the void fraction of particles in cell b, $V_{p,a}$ is the volume of particles a, $V_{cell,b}$ is the volume of cell b, $\mathbf{F}_{\mathrm{pf},a}$ is the solid–liquid interaction force of particles a, and n_b is the number of particles in cell b. This method is only applicable to the case where the cell contains multiple particles. When the particle size is larger than the mesh size, the error of the method will be very large, even void fraction of particles is larger than 1 in a single cell.[38] Therefore, to solve this problem, we proposed the VMDF. First, the true mass distribution function (TMDF) for a particle is calculated as

$$M_{\mathrm{T}}(r) = \int_{|\boldsymbol{\gamma}|=0}^{r} m_{\mathrm{T}}(\boldsymbol{\gamma})\mathrm{d}\boldsymbol{\gamma}, \tag{20}$$

$$m_{\mathrm{T}}(\boldsymbol{\gamma}) = \begin{cases} |\boldsymbol{\gamma}| \le R, & \rho_{\mathrm{p}}, \\ |\boldsymbol{\gamma}| > R, & 0, \end{cases} \tag{21}$$

where $\boldsymbol{\gamma} = \mathbf{x} - \mathbf{p}$, $\mathbf{p}$ is the center vector of particle position, $\mathbf{x}$ is a vector at any position in the flow field, R is the particle radius, and $m_{\mathrm{T}}(\boldsymbol{\gamma})$ is the true density distribution function (TDDF). The virtual density distribution function (VDDF) is defined as

$$m_V(\boldsymbol{\gamma}) = \frac{4}{3}\pi R^3 \rho_{\mathrm{p}} \varphi(\boldsymbol{\gamma}, \tau), \tag{22}$$

$$M_V(\infty) = \frac{4}{3}\pi R^3 \rho_{\mathrm{p}} = M_T(\infty), \tag{23}$$

where $m_V(\boldsymbol{\gamma})$ is the VDDF and $M_V(\boldsymbol{\gamma})$ is the VMDF.

As shown in Fig. 1, the void fraction of particles in at cell a is

$$\begin{aligned} \alpha_{\mathrm{p}}(\mathbf{x}_a) &= \frac{1}{V_{\mathrm{cell}}(b)} \int_{|\boldsymbol{\gamma}| \in V_{\mathrm{cell}}(a)} \frac{1}{\rho_{\mathrm{p}}} m_{\mathrm{V}}(\boldsymbol{\gamma}) \mathrm{p}\boldsymbol{\gamma} \\ &= \int_{|\boldsymbol{\gamma}| \in V_{\mathrm{cell}}(a)} \frac{4}{3} \frac{\pi R^3}{V_{\mathrm{cell}}(b)} \frac{1}{(4\pi\tau)^{\frac{3}{2}}} \exp\left(-\frac{\boldsymbol{\gamma}^2}{4\tau}\right) \mathrm{p}\boldsymbol{\gamma} \\ &= \int_{|\boldsymbol{\gamma}| \in V_{\mathrm{cell}}(a)} \frac{\alpha_{\mathrm{p,PCM}}(\mathbf{x}_J)}{(4\pi\tau)^{\frac{3}{2}}} \exp\left(-\frac{\boldsymbol{\gamma}^2}{4\tau}\right) \mathrm{p}\boldsymbol{\gamma}, \end{aligned} \tag{24}$$

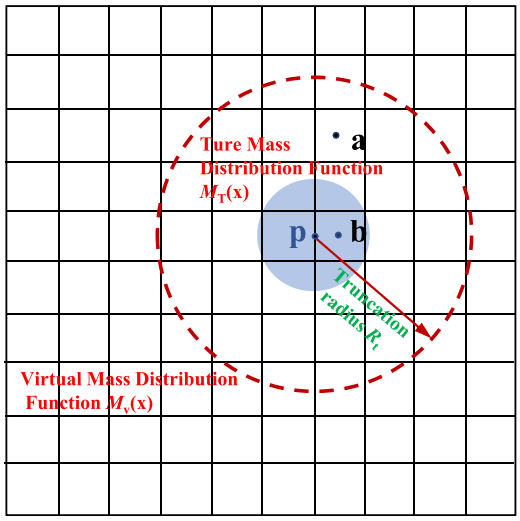

FIG. 1. The virtual mass distribution function.

where $V_{\mathrm{cell}}(a)$ and $V_{\mathrm{cell}}(b)$ are the volumes of cell a and b. $\mathbf{x}_a$ and $\mathbf{x}_b$ are the center vectors of the cell a and b. $\alpha_{\mathrm{p,PCM}}(\mathbf{x}_b)$ is the void fraction of particles in cell b. Based on the Green's function, Eq. (24) is the solution of Eq. (25):

$$\begin{cases} \dfrac{\partial \varphi(\boldsymbol{\beta}, \tau)}{\partial \tau} = \nabla^2 \varphi(\boldsymbol{\beta}, \tau), \\ \varphi(\boldsymbol{\beta}, \tau)|_{\tau=0} = \alpha_{\mathrm{p,PCM}}(\mathbf{x}_b)\delta(\mathbf{x}_b). \end{cases} \tag{25}$$

For the fluid–particle interaction forces $\mathbf{f}_{\mathrm{pf}}$, it is necessary to disperse the solid–liquid momentum exchange source term of coarse particles into the surrounding cells:

$$\mathbf{f}_{\mathrm{p}}(\varsigma) = \mathbf{f}_{\mathrm{p,PCM}}(\mathbf{x})\varphi(\mathbf{x} - \varsigma, \tau), \tag{26}$$

where ς is the position vector of any point in the flow field. $\mathbf{f}_{\mathrm{p,PCM}}$ is the momentum exchange source term. Similar to Eq. (24), Eq. (26) can be converted into the following equation:

$$\begin{cases} \dfrac{\partial \mathbf{f}_{\mathrm{p,PCM}}}{\partial \tau} = \nabla^2 \mathbf{f}_{\mathrm{p,PCM}}, \\ \mathbf{f}_{\mathrm{p,PCM}}|_{\tau=0} = \mathbf{f}_{\mathrm{p,PCM}}(\mathbf{x})\delta(\mathbf{x}), \end{cases} \tag{27}$$

where $\mathbf{x}$ is the center vector of all cells occupied by particle p. More details about VMDF can be found in Refs. 23 and 38.

E. Algorithm

The semi-resolved CFD-DEM has been implemented into the open-source code CFDEM,[14,38] which is divided into the OpenFOAM for the CFD part and LIGGGHTS for the DEM part. The specific algorithm is introduced as follows:

(1) The positions and velocities of the particles are obtained within a specific time step in the LIGGGHTS and then passed to the OpenFOAM.

(2) Particle void fraction and particle–fluid interaction forces are solved based on the positions and velocities of the particles.
(3) The flow field is solved based on the PISO (pressure-implicit with the splitting of operators) algorithm[48] using the particle void fraction and particle–fluid interaction forces.
(4) The force of the fluid acting on the particles is transferred back to the LIGGGHTS.

For OpenFOAM, the flow field is solved based on the finite volume method (FVM), so all variables, such as the fluid velocity, pressure, and void fraction, are stored in the center of the CFD cells. When integrating the convection and diffusion terms, it is necessary to use variables on the cell surfaces to calculate fluxes. We use the pressure-implicit with the splitting of operators (PISO) algorithm[48] for the fluid phase equations with pressure corrections and non-orthogonal flux corrections in the OpenFOAM. The second-order upwind scheme is employed in the discretizations of momentum and turbulent kinetic energy equations, and the implicit Euler discretization scheme is used to discretize the transient term. The source terms are calculated by all variables in the center of the CFD cells. For LIGGGHTS, the positions and velocities of the particles are obtained based on Newton's second law.

III. COMPUTATIONAL SETTINGS

As shown in Fig. 2, a fluidized bed is set in a vertical pipe with a diameter of 50 mm and a length of 0.6 m. The computational geometry is divided by a hexahedral mesh with about 40 500 cells using the mesh generation utility BlockMesh included in OpenFOAM. The mesh size is $3.33 \times 3.33 \times 3.33$ in the x, y, and z directions, respectively. As shown in Table II, the size of the two particles is larger than the mesh size, and the other particle sizes are larger than the mesh size. This fully demonstrates the wide applicability of the semi-resolved CFD-DEM, that is, it can be applied to both particle sizes larger than the mesh size and particle sizes smaller than the mesh size.

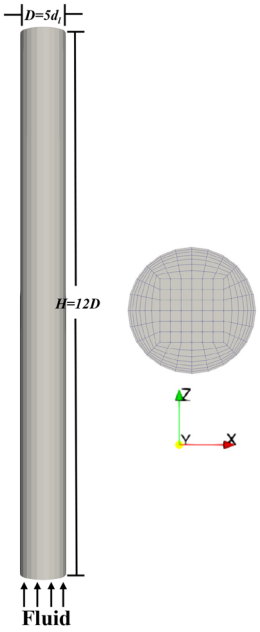

FIG. 2. Computational geometry.

A. Numerical setting

The fluidized bed is filled with two species of spherical particles with a density of $\rho_p = 2600\,\mathrm{kg/m^3}$. The two species of particle sizes are $d_1 = 10$ (species 1) and $d_2 = 2$–7 mm (species 2). The ratios of two species of particles are shown in Table II. Fluid defaults are room temperature water with a density of $\rho_f = 1000\mathrm{kg/m^3}$ and a viscosity of $\nu_f = 1.0 \times 10^{-6}\mathrm{m^2/s}$. All parameters used in the numerical simulation are shown in Table III. First, we analyze the particle mixing and segregation behaviors with different size ratios. In this part, the size of species 1 is a constant value, and the particle size in species 2 changes. It is worth noting that the ratio of the particle size in species 2 to pipe diameter d_2/D is 0.04–0.14 in Table II, obviously which has both fine and coarse particles in species 2 according to the range of coarse particles $d_p/D \geq 0.1$.[15,16] To better understand the differences in dynamic characteristics between coarse and fine particles, we only concentrate on the dynamic characteristics in species 2 after the segregation of species 1 and 2. Moreover, to understand the causal relationship of the differences, the Stokes number St_p, which characterizes the motion of particles, is introduced as follows:[49,50]

$$St_p = \frac{\rho_p d_2^2}{18\mu_f}\frac{u_f}{D}, \tag{28}$$

where d_2 is particle diameter in species 2. μ_f is dynamic viscosity coefficient of fluid. u_f is upward fluid velocity. D is the pipe diameter. The Stokes number St_p is defined as the ratio of particle response time to the fluid characteristic timescale. It reflects the inertial effects of particles, which suggests that the larger Stokes number the more likely particles will undergo more frequent collisions.[51]

As shown in Table II, the particle sizes d_2 in species 2 are as follows: 2, 3, 4, 5, 6, and 7 mm, corresponding to St_p are 1.96, 4.42, 7.86, 12.28, 17.68, and 24.06, respectively. That is, the smaller Stokes number St_p corresponding to fine particles (2, 3, and 4 mm) is 1.96, 4.42, and 7.86, and the larger Stokes number St_p corresponding to coarse particles (5, 6, and 7 mm) is 12.28, 17.68, and 24.06.

B. Boundary conditions and time step

The vertical pipe has three boundaries: the inlet, the outlet, and the wall. At the inlet of the pipe (bottom boundary), the fluid velocity is a given value u_0. The pipe wall is no-slip boundary conditions, so the normal and tangential fluid velocities are set to zero. At the outlet

TABLE II. Settings of particle size and the ratio of binary particles.

Case	d_1 (mm)	d_2 (mm)	d_1/d_2	d_2/D	St_p
1	10	7	1.43	0.14	24.06
2	10	6	1.67	0.12	17.68
3	10	5	2.00	0.10	12.28
4	10	4	2.50	0.08	7.86
5	10	3	3.33	0.06	4.42
6	10	2	5.00	0.04	1.96

of the pipe (upper boundary), the fluid pressure is specified and the velocity gradient of the fluid is set as zero. As initial conditions, the fluid velocity is zero, and the particles fall freely to the bottom of the pipe. After particles are in a steady state, then particles move upward together under the action of the fluid with a given inlet velocity. The packing bed consists of two layers (species 1 and 2) at the bottom of the vertical pipe, where the top layer is species 1 and the bottom layer is species 2.

The numerical model is solved in Sec. II based on CFDEM, where the flow field and particle motion are solved by the CFD and DEM models, respectively. Thus, the DEM module (t_{DEM}) and the CFD module (t_{CFD}) have independent time steps. The data are exchanged once after a certain time step. To keep the DEM time step less than 10% the Rayleigh time,[52] the time steps are calculated by

$$t_{DEM} = \frac{0.5\pi d_p}{0.163\nu + 0.8766}\sqrt{\frac{2\rho_p(1+\nu)}{Y}}, \tag{29}$$

where ν is Poisson's ratio and Y is Young's modules. The time step of the DEM model is set as $t_{DEM} = 1 \times 10^{-5}$ s. The time step of the CFD model is generally 10–100 times that of the DEM model,[53] so the time step of the CFD model is set as $t_{CFD} = 5 \times 10^{-4}$ s.

IV. MODEL VALIDATION

The paper adopts the semi-resolved CFD-DEM based on the CFDEM. This part will briefly verify the reasonability of the numerical model in a fluidized bed. The pressure drop equation related to the inlet fluid velocity is proposed by Ergun and Orning[54] as follows:

$$\frac{\Delta p}{L} = 150\frac{(1-\alpha_f)^2}{\alpha_f^3}\frac{\nu_f u_z}{d_p^2} + 1.75\frac{1-\alpha_f}{\alpha_f^3}\frac{\rho_f u_z^2}{d_p}, \tag{30}$$

where α_f is the void fraction of fluid. u_z is the inlet fluid velocity. Fluidization is a suspension of particles in a vertical pipe under the action of the upward inlet fluid. The pressure drop Δp increases with the increase in inlet velocity in a fixed bed. When the pressure drop equals the buoyant weight of the solid particles per unit area of the bed, the fixed bed begins to expand. In this case, the inlet fluid velocity is called the minimum fluidization velocity. The minimum fluidization velocity[54] is calculated by

$$u_m = \begin{cases} Re_m < 1000, & \sqrt{\dfrac{(\rho_p - \rho_f)d_p g\alpha_f^3}{1.75\rho_f}}, \\ Re_m \geq 1000, & \dfrac{d_p^2(\rho_p - \rho_f)g\alpha_f^3}{150\mu_f(1-\alpha_f)}, \end{cases} \tag{31}$$

$$Re_m = \frac{u_m d_p}{\nu_f}, \tag{32}$$

where Re_m is the particle Reynolds number and u_m is the minimum fluidization velocity.

As shown in Fig. 3, a fluidized bed is formed in a vertical pipe, where the bed consists of glass balls with a diameter of 5 mm and a density of 2600 kg/m^3. Other parameters in the numerical simulation are shown in Table III. In the initial, these particles are freely accumulated at the bottom of the pipe. Then, the inlet fluid velocity increases linearly at the bottom. Figure 4 shows the variation of pressure drop

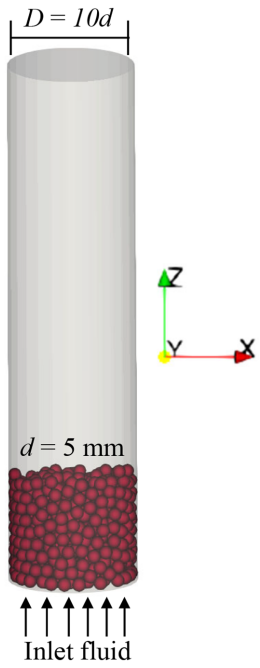

FIG. 3. The geometry of the fluidized bed in a vertical pipe.

with inlet fluid velocity in the fluidized bed. The analytic pressure drop is obtained from Eq. (30). As shown in Fig. 4, the numerical simulation results are in good agreement with the analysis results. Based on the above, we further verify the minimum fluid velocity of particles with

TABLE III. All parameters used in the numerical simulation.[4,17,23]

Parameters	Values
The parameters of vertical pipe	
Pipe diameter, D (mm)	50
Pipe length, H (m)	0.6
Particle parameters	
Particle density, ρ_p (kg/m^3)	2600
Large particles' diameter, d_1 (mm)	10
Small particles' diameter, d_2 (mm)	2–7
Young's modulus, Y (Pa)	1.0×10^8
Poisson's ratio, ν	0.23
Coefficient of restitution, μ_c	0.5
Sliding friction coefficient, μ_s	0.5
Water parameters	
Fluid density, ρ_f (kg/m^3)	1000
Fluid viscosity, ν_f (m^2/s)	1.0×10^{-6}
Upward fluid velocity, u_0 (m/s)	0.17
Simulation parameters	
CFD time step, t_{CFD} (s)	5.0×10^{-4}
DEM time step, t_{DEM} (s)	1.0×10^{-5}

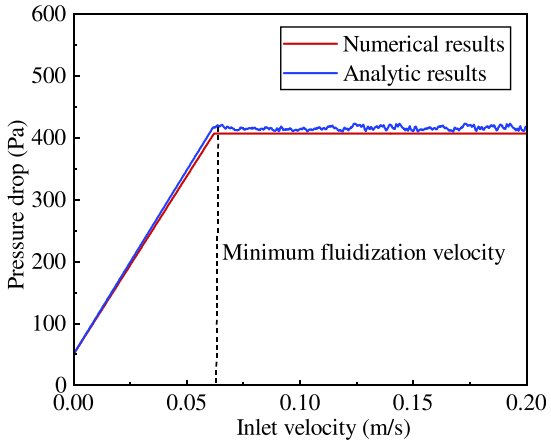

FIG. 4. The variation of pressure drop with inlet fluid velocity in a fluidized bed.

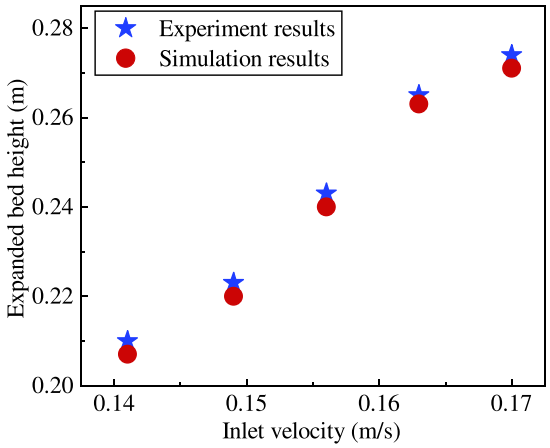

FIG. 6. The expanded bed height between numerical and experimental results.

different sizes by comparing analytic and numerical results. The particle sizes are 3, 4, 5, 6, and 7 mm and particle density is 2600 kg/m^3. Finally, a linearly varying fluid velocity is set at the inlet of the pipe. When the pressure drop is basically stable, the inlet fluid velocity is the minimum fluidization velocity. As shown in Fig. 5, the results of numerical simulation are close to the analytic results.

Finally, we calculate the expansion height in a fluidized bed and compare it with the experimental results (Fig. 6).[4] The fluidized bed was formed in a cylinder with a diameter of 50 mm and a height of 0.3 m, consisting of two particles with the same particle density of 2230 kg/m^3: 120 g species 1 with the diameter 8 mm and species 2 with the diameter 3 mm. Fluid defaults to room temperature water, with a density of $\rho_f = 1000\text{kg/m}^3$ and a viscosity of $\mu_f = 0.001$ kg/(ms). At the inlet of the pipe, the fluid velocity is set to 0.141, 0.149, 0.156, 0.163, and 0.170 m/s, respectively. As initial conditions, the packing bed consists of two layers (species 1 and 2) at the bottom of the vertical pipe, where the top layer is species 1 and the bottom layer is species 2, and then move upward together under the action of the fluid. As shown in Fig. 6, the numerical simulation results are in good agreement with the experimental results.

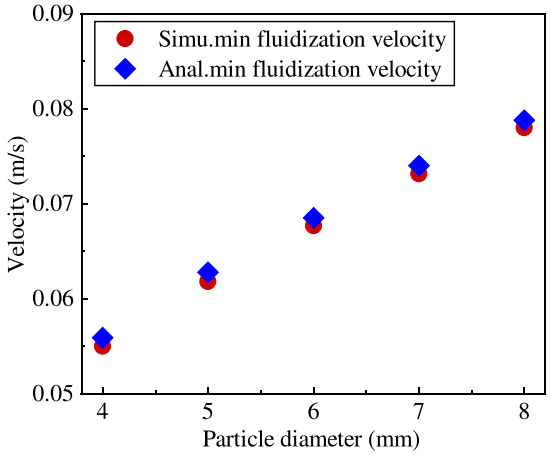

FIG. 5. The minimum fluidization velocity between numerical and analytic results at different particle sizes.

V. RESULTS AND DISCUSSION

To better explore the time evolution of particulate flows, the ensemble-averaged variable of the particle is defined as

$$\langle\langle\{\cdot\}_i\rangle\rangle = \frac{1}{N_p}\sum_{i=1}^{N_p}\{\cdot\}_i, \tag{33}$$

where $\{\cdot\}_i$ is the variable of particle i, such as particle velocity.

Figure 7 shows the ensemble-averaged vertical velocities of all particles with time at $St_p = 24.06$. In this paper, the time is normalized by the particle turnover time ($\tau_p = d_p/u_0$), and the ensemble-averaged particle velocity is normalized by the fluid velocity u_0. As

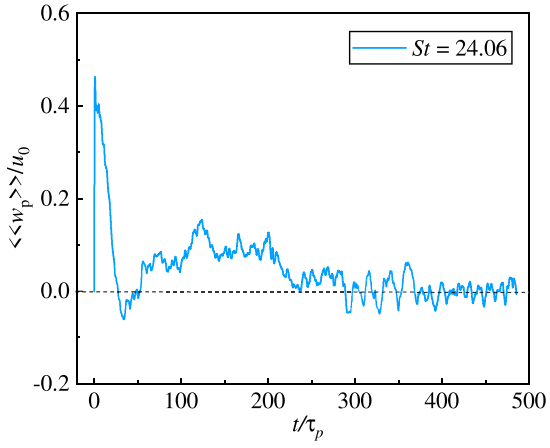

FIG. 7. Time series of the ensemble-averaged vertical velocity of the whole particles $\langle\langle w_p\rangle\rangle$ at $St_p = 24.06$. The statistical equilibrium is about $t = 370\tau_p$, where $\tau_p = d_p/u_0$ is the particle turnover time.

shown in Fig. 7, the particle velocity increases initially when species 1 and 2 are mixed, because the average drag force of the fluid acting on the particles is greater than the submerged gravity. Eventually, the average drag force and submerged gravity are balanced, and then, the particles are in statistical equilibrium. It can be seen from Fig. 7 that the statistical equilibrium is reached after t = 370 τ_p at $St_p = 24.06$. Thus, the maximum simulation time is $t_{max} = 728 - 2550\tau_p$ to ensure statistical stationary results, which depends on different Stokes numbers St_p.

Time-averaged statistics are calculated by Eq. (34), and more than 240 τ_p are calculated,

$$\overline{\{\cdot\}} = \frac{1}{240\tau_p}\int_{t_{max}-240\tau_p}^{t_{max}} \{\cdot\}\mathrm{d}t, \tag{34}$$

where $\{\cdot\}$ is the related variable in the simulation. It is worth noting that the time and velocity mentioned below are normalized variables.

First, in Sec. V A, we analyze the mixing and segregation behaviors of species 1 and 2 at different size ratios. For species 2, there are both fine and coarse particles. Thus, after the segregation of species 1 and 2, we only quantitatively study the differences in dynamics of species 2 from fine to coarse particles in Secs. V B and V C and reveal the mechanism for the differences in Sec. V D.

A. The particle mixing and segregation behaviors

This section mainly qualitatively analyzes the particle mixing and segregation behaviors over time when the particle size ratios are 2.5 and 1.43, respectively. As shown in Figs. 8 and 9, red represents species 1, and blue represents species 2. In the initial state, the top layer is species 1 and the bottom layer is species 2. Then, species 1 and 2 form the granular plug and rise as a whole under the action of the fluid, and particles fall gradually. Subsequently, species 2 starts to migrate through species 1. Finally, the phenomenon forms that species 2 is the top layer and species 1 is the bottom layer. All processes represent the layer inversion.[5,14] By comparing with the smaller size ratio (1.43) in

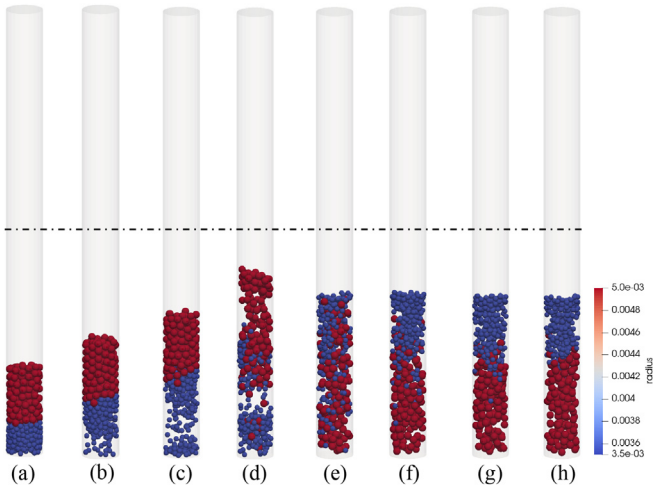

FIG. 9. Instantaneous snapshots of particle mixing and segregation at size ratio of 1.43. The corresponding normalized times are (a) 0.0, (b) 24.3, (c) 72.9, (d) 97.1, (e) 194.3, (f) 291.4, (g) 388.6, and (h) 485.7. Multimedia available online.

Fig. 9 (Multimedia view), at the larger size ratio (2.5) in Fig. 8 (Multimedia view), species 2 has migrated into species 1 when the plug is still rising, leading to a higher particle mixing degree. The particles are more aggregated in this case. Eventually, the granular plug is prominent at a larger size ratio (2.5) in Figs. 8(b)–8(d).

The network of contact forces is a contact force chain between particles, which can reflect the contact between particles and the constraint of the wall on particle motion.[17,34] Thus, when two particles with different size ratios are mixed, the evolution of the contact force network is explored. Figures 10 and 11 show the change in the network of contact forces when the size ratio is 2.5 and 1.43, respectively. When two particles are mixed at the larger size ratio (2.5), the contact

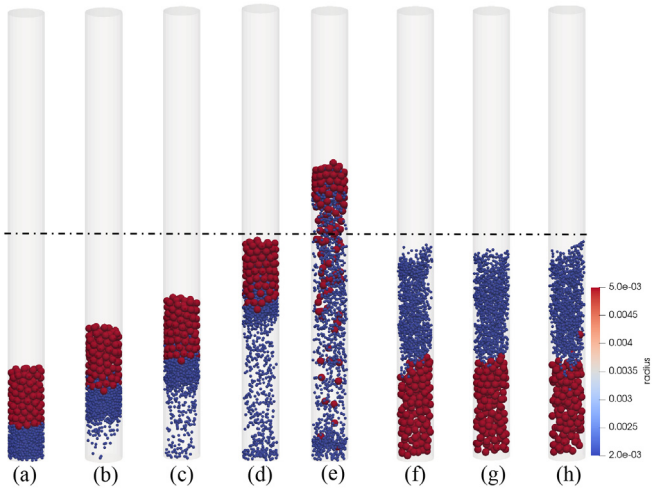

FIG. 8. Instantaneous snapshots of particle mixing and segregation at size ratio of 2.5. The corresponding normalized times are (a) 0.0, (b) 42.5, (c) 85.0, (d) 127.5, (e) 170.0, (f) 340.0, (g) 510.0, and (h) 680.0. Multimedia available online.

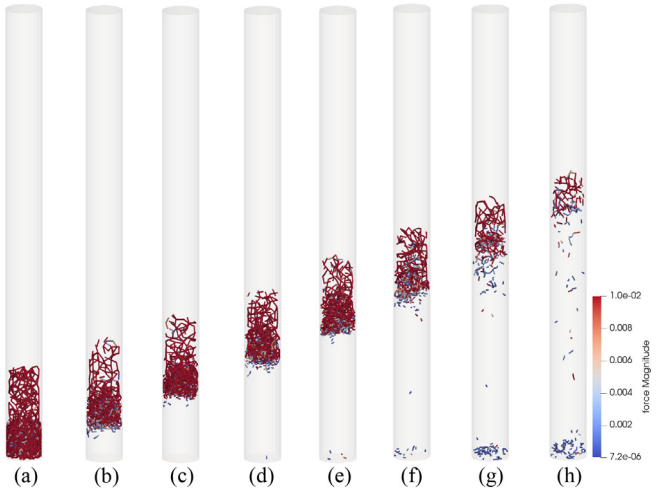

FIG. 10. Instantaneous snapshots of the network of contact forces at a size ratio of 2.5. The corresponding normalized times are (a) 0.0, (b) 17.0, (c) 34.0, (d) 51.0, (e) 68.0, (f) 85.0, (g) 102.0, and (h) 119.0.

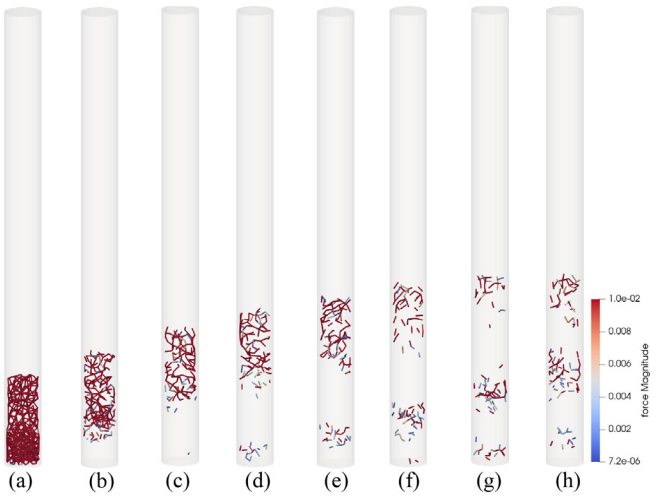

FIG. 11. Instantaneous snapshots of the network of contact forces at a size ratio of 1.43. The corresponding normalized times are (a) 0.0, (b) 9.7, (c) 19.4, (d) 29.1, (e) 38.85, (f) 48.6, (g) 58.3, and (h) 68.0.

chains are stronger in Fig. 10, corresponding to a prominent plug of Fig. 8. While the sizes of the two species of particles are closer (1.43), the contact chains and the plug are weaker in Figs. 9 and 11. Therefore, the wall has stronger constraints on the mixing of two particles with a larger size ratio, and the probability of the plug is higher in this case, easily leading to pipe blockage. The phenomenon is what we do not want to see. To ensure safety in realistic industry operations, it is recommended that the differences in particle sizes should not be too large possible when there are different particle sizes in a vertical pipe.

B. Velocity fluctuations

In the fluidized beds, the ensemble-averaged vertical velocity of the particles $\langle\langle w_p \rangle\rangle$ is a constant, which indicates that the particles are in an equilibrium state when the particle–fluid interaction force and submerge gravity are balanced.[1] However, some researchers found that the velocity fluctuations of particles and fluids are 10%–120% higher than the inlet fluid velocity due to particle–particle/wall collision forces.[1,23,24] Hence, in this section, particle and fluid velocity fluctuations are analyzed at different Stokes numbers St_p. To better analyze the effects of Stokes number St_p, the root mean square velocity is introduced as follows:

$$u_{rms,i} = \sqrt{\overline{\langle\langle u_i' u_i' \rangle\rangle}}, \tag{35}$$

where $u_i' = u_i - \langle\langle \bar{u}_i \rangle\rangle$ is the fluctuations of particle velocity in different directions (x, y and z). $\langle\langle \cdot \rangle\rangle$ is the ensemble-averaged particle variable in the simulation defined in Eq. (33). The overbar is time-averaged statistics defined in Eq. (34).

Figures 12(a) and 12(b) are the root mean square of particle and fluid velocity fluctuations (u_0) at different Stokes numbers St_p, respectively, normalized by inlet fluid velocity u_0. The $u_{rms,z}$ increases first and then decreases with increasing of Stokes number St_p. Also, $u_{rms,z}$ is greater than $u_{rms,x}$ and $u_{rms,y}$, which is because the particle motion mainly occurs in the z direction under the action of upward fluid, and the wall constrains the particle motion in the x and y directions. Similar to Fig. 12(a), we calculate the root mean square of fluid velocity fluctuations ($u_{f,rms}$) in different directions (x, y, and z) with St_p. On the whole, the trend of fluid velocity fluctuation is consistent with that of particles. It is very obvious that the particle velocity fluctuation is greater than the fluid velocity fluctuation no matter which direction. It is because particle collision leads to frequent instantaneous changes in particle velocity and then causes the particle velocity fluctuations to occur over timescales that are too short for the fluid to respond.

C. Autocorrelation and radial distributions

1. Autocorrelation

To better analyze the process of governing the fluctuating particle motions, this part discusses the change of instantaneous particle velocity fluctuation autocorrelation at a given time lag τ. The normalized autocorrelation[55,56] is as follows:

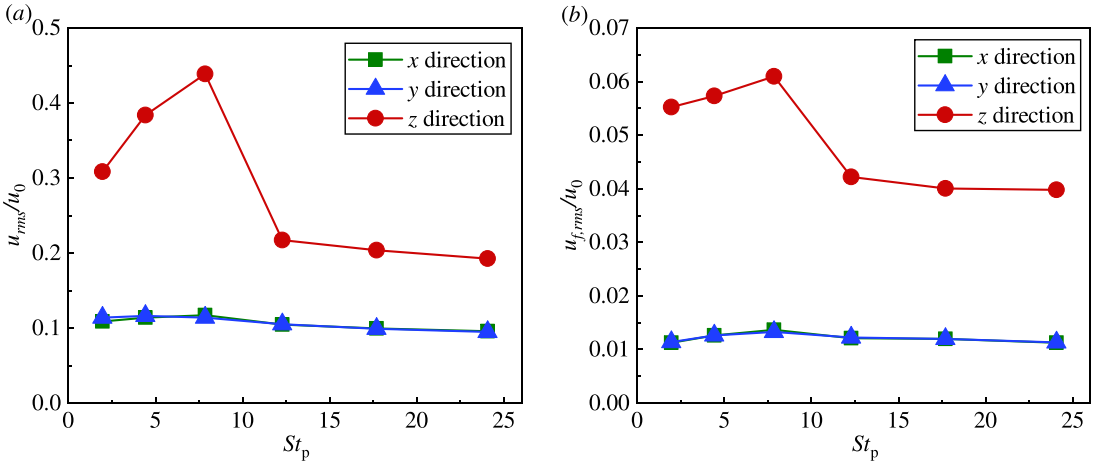

FIG. 12. The change of root mean square velocity normalized by inlet fluid velocity with different Stokes numbers St_p: (a) particle velocity and (b) fluid velocity.

$$R_{ii}(\tau) = \frac{\langle\langle u_i'(t_0)u_i'(t_0+\tau)\rangle\rangle}{\langle\langle u_i'(t_0)u_i'(t_0)\rangle\rangle}, \tag{36}$$

where t_0 is a selected time after species 1 and 2 are segregated and in equilibrium. i represents x, y, and z directions.

Figure 13 shows the change in instantaneous particle velocity fluctuation autocorrelation R_{ii} with time in different directions (R_{xx}, R_{yy}, and R_{zz}) and different Stokes number St_p. As shown in Fig. 13, the particle velocity remains a correlation of about 15–80 τ_p with different St_p. In addition, another significant feature is that the autocorrelation coefficient in the horizontal direction (x and y directions) decreases faster than that in the vertical direction (z direction), which also means that the particle velocity decorrelates in the horizontal direction faster than that in the vertical direction. Similar research results can be found in Refs. 1 and 57. It is likely that under the action of the upward fluid, random particle motion is preferentially excited in the vertical direction, and the wall constrains particle motion in the horizontal direction.

The autocorrelation timescale of particle velocity fluctuations is as follows:

$$\mathscr{R}_i = \lim_{\tau\to\infty}\int R_{ii}(\tau)\mathrm{d}\tau. \tag{37}$$

Unfortunately, the time is limited in numerical simulation. Thus, the computed integral timescale is approximated with

$$\mathscr{R}_{i,c} = \lim_{\tau\to t_f}\int R_{ii}(\tau)\mathrm{d}\tau, \tag{38}$$

where t_f is the simulation time. To calculate the computed integral timescale, we define $N_\tau = \frac{u_0 t_f}{d_p}$.

Figure 14 is the integral timescale of the particle velocity fluctuation autocorrelation R_{ii} as a function of τ/τ_p in x and z directions at $St_p = 7.86$. As shown in Fig. 14, $\mathscr{R}_x, c$ and $\mathscr{R}_z, c$ first increase with the increase in normalized time (τ/τ_p) and then reach a relatively stable value due to the wavelike autocorrelations. The average time value is calculated by

$$E(\mathscr{R}_{i,c}) = \frac{1}{N_{\tau,s}}\sum_{j=N_\tau-N_{\tau,s}}^{N_\tau}\mathscr{R}_{i,c}^j, \tag{39}$$

where N_τ is all data after the $\mathscr{R}_{i,c}$ reaches a steady state. $N_{\tau,s}$ is the minimum N_τ for the $\mathscr{R}_{i,c}$ to reach a steady state. $E(\mathscr{R}_{i,c})$ is the average value of the $\mathscr{R}_{i,c}$. That is, t_f is the simulation time when $\mathscr{R}_{i,c}$ reaches stability. To reduce the error, t_f selects the maximum simulation time in our cases.

Then, the normalized autocorrelation length scale is calculated: $l_i^* = l_i/d = u_{rms,i}E(\mathscr{R}_{i,c})/d$, which represents the length scale that the particle velocity fluctuation is still correlated.[1] When $l^* > 1$, the propagation length of particle velocity fluctuation is larger than a particle diameter. While $l^* < 1$, the fluctuation length of particle velocity is less than a particle diameter. Figure 15(a) shows the changes in autocorrelation length of particle velocity fluctuation with different St_p in x and z directions. In the z direction, the normalized autocorrelation length is $l_z^* > 1$ at smaller St_p (1.96, 4.42, and 7.86), that is, the velocity fluctuation propagates faster than a particle diameter, indicating the

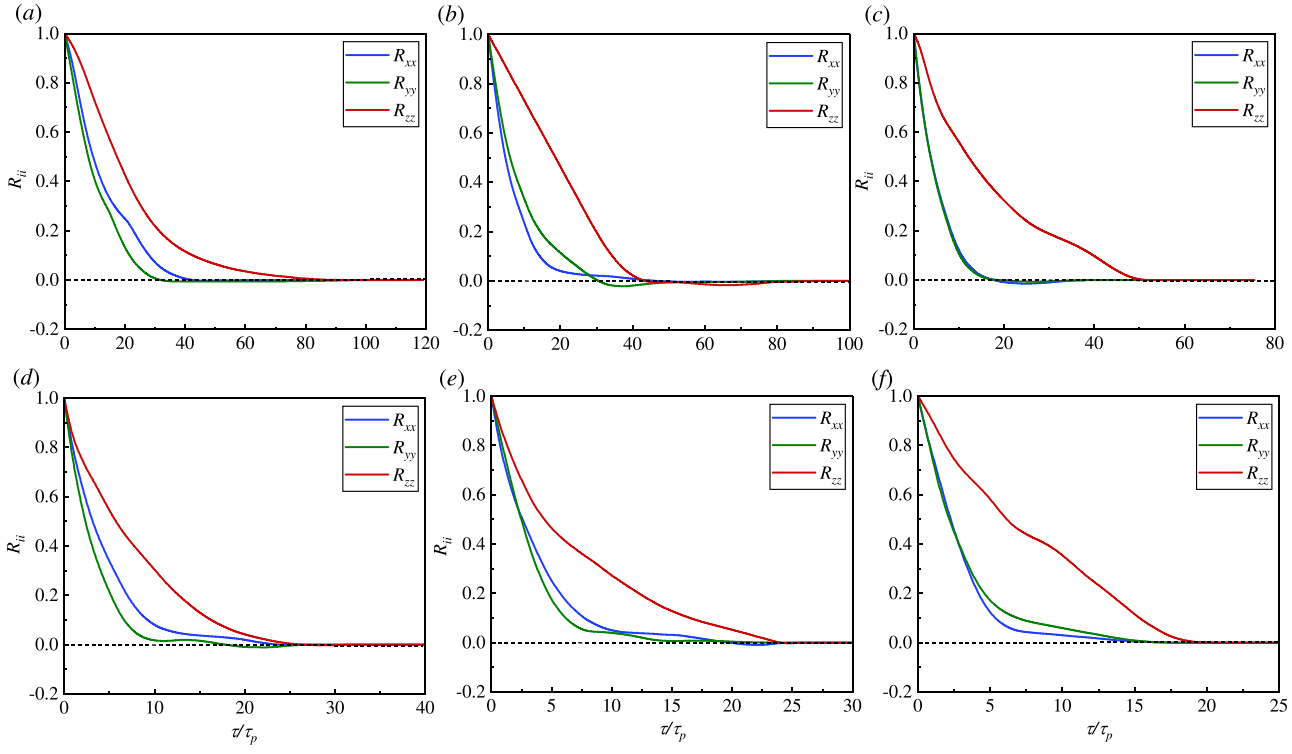

FIG. 13. The change in instantaneous particle velocity fluctuation autocorrelation R_{ii} with time in different directions (R_{xx}, R_{yy}, and R_{zz}) and different Stokes numbers:(a) $St_p = 1.96$, (b) $St_p = 4.42$, (c) $St_p = 7.86$, (d) $St_p = 12.28$, (e) $St_p = 17.68$, and (f) $St_p = 24.06$.

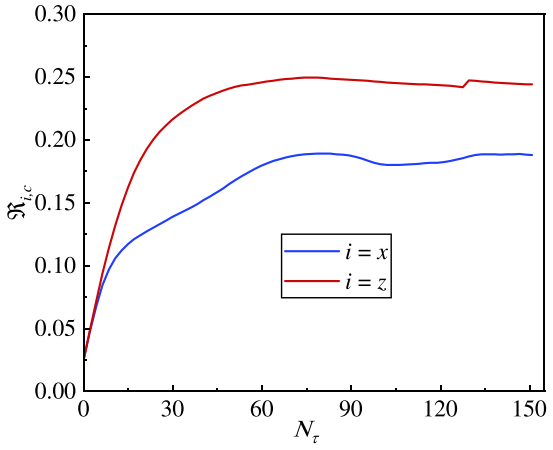

FIG. 14. The integral timescale of the particle velocity fluctuation autocorrelation R_{ii} as a function of τ/τ_p in x and z directions at $St_p = 7.86$.

influence of mean flow is prominent in these cases. While at larger St_p (12.28, 17.68, and 24.06), the normalized autocorrelation length is $l_z^* < 1$. It is due to the increase in particle inertia with the increase in St_p, the particle velocity fluctuation is dominated by particle collision. This is also a clear difference between fine and coarse particles. It is worth noting smaller Stokes number St_p corresponds to fine particles (2–4 mm), and the larger Stokes number St_p corresponds to coarse particles (5–7 mm). In addition, l_x^* decreases with the increase in St_p. It is because the increase in the St_p brings the higher wall constraint on particle motion in the horizontal directions from fine particles to coarse particles, which is consistent with Figs. 12 and 13. Figure 15(b) represents the ratio of transverse and axial autocorrelation length, which indicates anisotropy. As shown in Fig. 15(b), the ratios of transverse and axial autocorrelation length increase, that is, the anisotropy gradually decreases with the increase in St_p.

2. Radial distribution function (RDF)

To explore the relationship between anisotropy and Stokes number St_p, we use the pair probability distribution function proposed by Yin and Koch.[58] It is as follows:

$$P(\boldsymbol{r}) = \frac{0.25\pi D^2 H^*}{N_p^2}\left\langle\left\langle \sum_{i=1}^{N_p}\sum_{j=1,j\neq i}^{N_p}\delta(\boldsymbol{r}-\boldsymbol{r}_{ij})\right\rangle\right\rangle, \tag{40}$$

where $\boldsymbol{r}_{ij} = (r_{ij}, \theta_{ij})$ is the vector connecting particle i and particle j. $\langle\langle\cdot\rangle\rangle$ represents the ensemble average in the simulation. H^* is the expansion height of species 2 after species 1 and 2 are segregated. δ is the Dirac function as follows:

$$\delta(\boldsymbol{r}-\boldsymbol{r}_{ij}) = \begin{cases} 1, & \boldsymbol{r} = \boldsymbol{r}_{ij}, \\ 0 & \text{other}, \end{cases} \tag{41}$$

where $r_{ij} = ||\boldsymbol{x}_i - \boldsymbol{x}_j||$. $\boldsymbol{x}_i$ and $\boldsymbol{x}_j$ are the position center coordinates of the particle i and j, respectively. The θ_{ij} is calculated as follows:

$$\theta_{ij} = \begin{cases} \arccos(|z_i - z_j|/r_{ij}), & z_i - z_j < 0, \\ \arcsin(|z_i - z_j|/r_{ij}), & z_i - z_j \geq 0, \end{cases} \tag{42}$$

where z is the coordinate of a particle in z direction.

Then, the radial distribution function (RDF) $g(r, \theta)$ is calculated based on the pair probability distribution function $P(\boldsymbol{r})$, which indicates the density of particle pairs as a function of radial segregation.[58,59] It is in three ranges: the entire range $0 < \theta < \pi/2$, the vertical section $0 < \theta < \pi/12$, and the horizontal section $5\pi/12 < \theta < \pi/2$. Figure 16 shows the angular variation of the RDF at the three ranges with different Stokes numbers St_p. As shown in Fig. 16, it is obvious that there are two peaks at $r/d_p = 1$ and $r/d_p = 2$, indicating that particles are likely to appear in the two positions. Moreover, when $r/d_p = 1$, the entire RDF at smaller St_p (1.96, 4.42, and 7.86) is smaller than the RDF at larger St_p (12.28, 17.68, and 24.06). While $r/d_p = 2$, the entire RDF at smaller St_p is larger than the RDF at larger St_p. Figure 17 shows the change of $g(r/d_p = 2)$ at

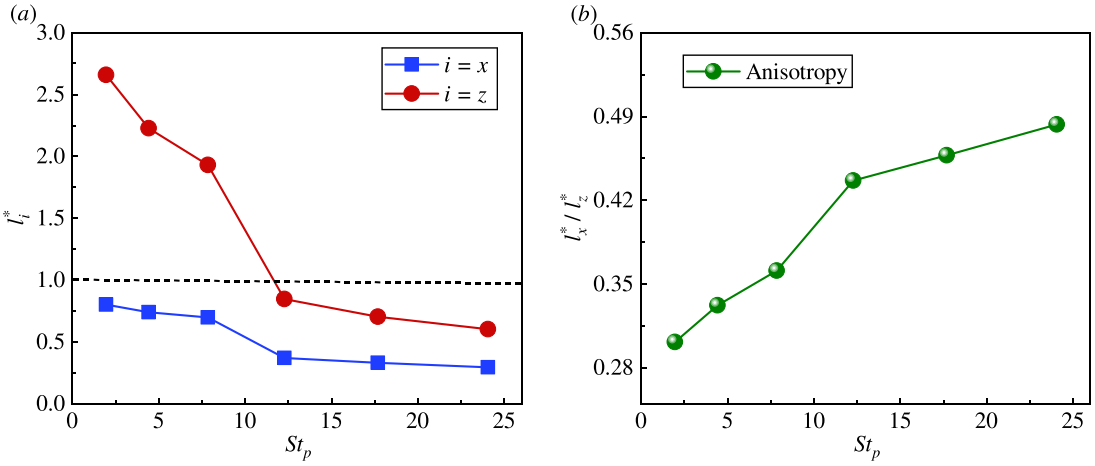

FIG. 15. The normalized autocorrelation length scale at different Stokes numbers St_p: (a) autocorrelation length scale in x and z directions and (b) the ratio of transverse and axial autocorrelation length (l_x^*/l_z^*) indicate anisotropy.

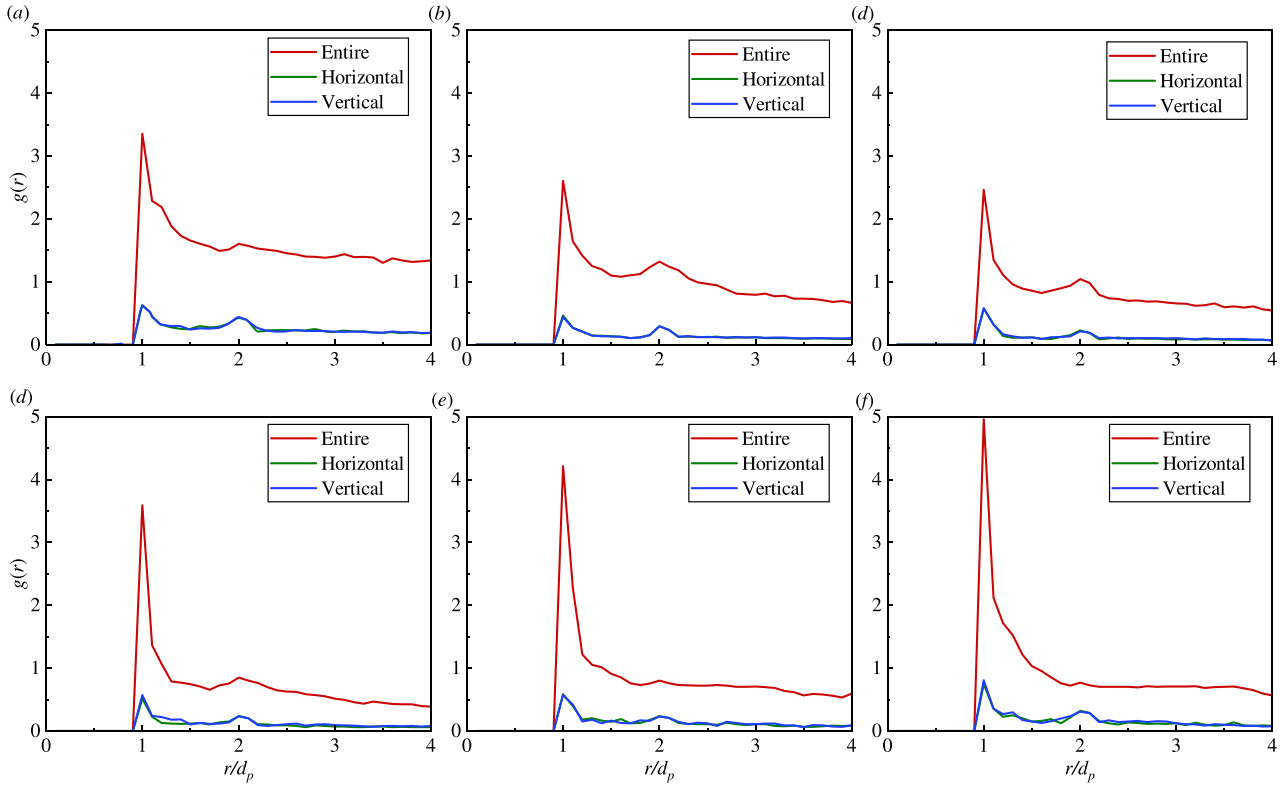

FIG. 16. The angular variation of the radial distribution functions at different Stokes numbers St_p: (a) $St_p = 1.96$, (b) $St_p = 4.42$, (c) $St_p = 7.86$, (d) $St_p = 12.28$, and (e) $St_p = 17.68$, and (f) $St_p = 24.06$. The red lines represent the average over the entire range $0 < \theta < \pi/2$; the green lines are the horizontal sector $5\pi/12 < \theta < \pi/2$; the blue lines are the vertical sector $0 < \theta < \pi/12$.

different Stokes numbers St_p. It is obvious that two flow regimes are found after linear regression. They are regime1 (smaller St_p) and regime2 (larger St_p), which suggests that the particle collision is prominent at the larger St_p again. Next, we will analyze its potential mechanism in detail.

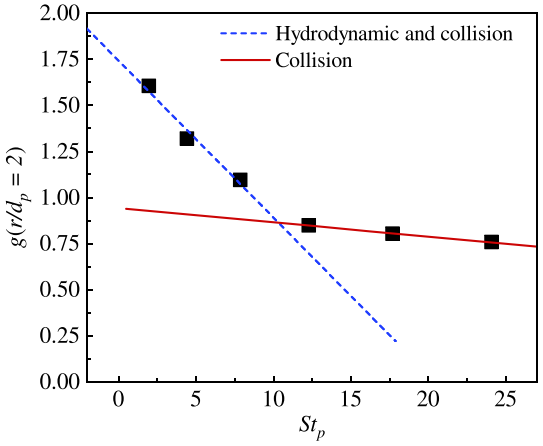

FIG. 17. The variation of the pair probability distribution functions $[g(r/d = 2)]$ at different Stokes numbers St_p. Different lines obtained by linear regression indicate different regimes.

D. Particle collisions and fluid–particle interactions

To better understand the mechanisms for differences in dynamic characteristics between fine particles and coarse particles, we calculate the collision stress σ_{co}, hydrodynamic stress σ_{hy} to quantify the particle–particle/wall collisions, and particle–fluid interactions. The collision stress σ_{co} and hydrodynamic stress σ_{hy} are as follows:

$$\sigma_{co} = \frac{1}{N_t N_p} \sum_{t=1}^{N_t} \sum_{n=1}^{N_p} \frac{|\boldsymbol{f}_c|_n^t}{\pi d_p^2}, \tag{43}$$

$$\sigma_{hy} = \frac{1}{N_t N_p} \sum_{t=1}^{N_t} \sum_{n=1}^{N_p} \frac{|\boldsymbol{f}_{pf}|_n^t}{\pi d_p^2}, \tag{44}$$

where N_p is the number of particles and N_t is the number of time samples in equilibrium. The stress is normalized by $d_p{}^2/\rho_f \nu_f^2$, and the normalized stress is expressed as $\hat{\sigma}$.

Figure 18 shows the normalized hydrodynamic stress and collision stress variation at different Stokes numbers St_p. As shown in Fig. 18, both the $\hat{\sigma}_{co}$ and $\hat{\sigma}_{hy}$ increase with the increase in St_p. However, the collision stress $\hat{\sigma}_{co}$ increases faster. It is due to the increase in particle inertia with the increase in St_p, and then, particle collision frequency increases (see from Fig. 19), leading to the instability of particle motion, for smaller St_p, 1.96, 4.42, and 7.86, $\hat{\sigma}_{hy} > \hat{\sigma}_{co}$. This shows that the hydrodynamic effects are slightly larger than the collisions in this case, but the difference is small. It corresponds to regime1 (smaller St_p) in

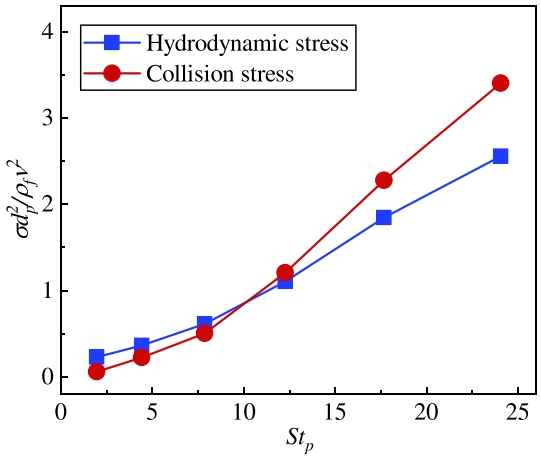

FIG. 18. The variation of the normalized hydrodynamic stress and collision stress at different Stokes numbers St_p.

Fig. 17, indicating that the hydrodynamic and collision stresses are equally important. For larger St_p, 12.28, 17.68, and 24.06, it is obvious that $\tilde{\sigma}_{hy} < \tilde{\sigma}_{co}$, corresponding to regime2 (larger St_p), which suggests that the collisions dominate in the case. In this paper, the smaller St_p (1.96, 4.42, and 7.86) to larger St_p (12.28, 17.68, and 24.06) corresponds to fine particles (2–4 mm) to coarse particles (5–7 mm), respectively. Therefore, the reason for the differences in particle dynamics between fine and coarse particles is that the effects of collisions are greater than that of the hydrodynamic effects with the increase in St_p.

To further analyze the collisions, the time and ensemble average collision frequency f_{re} are calculated as follows:

$$f_{re} = \frac{1}{N_t N_p} \sum_{t=1}^{N_t} \sum_{n=1}^{N_p} N_{re,n}^t, \tag{45}$$

where $N_{re,n}^t$ is the number of collisions between particle n and other particles at time t. The collisions occur when the distance between two particle centers is less than a particle diameter d_p.

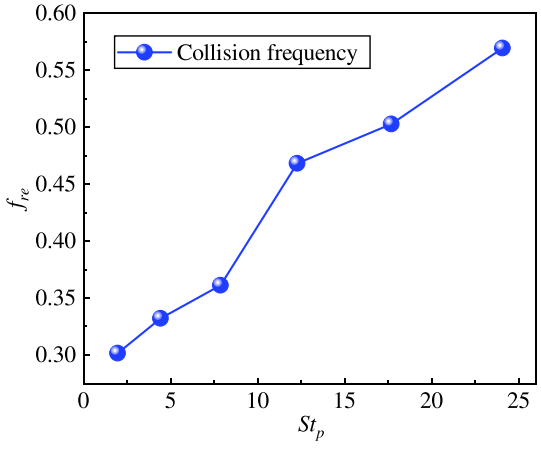

FIG. 19. The change in the average collision frequency f_{re} over different Stokes numbers St_p.

Figure 19 shows the change in the average collision frequency f_{re} with different Stokes numbers St_p. As shown in Fig. 19, similar to the normalized collision stress, the collision frequency increases with the increase in St_p. It evidences that the collision is prominent at larger St_p. The collisions between particles can transfer momentum from the vertical direction to the horizontal direction, which leads to horizontal particle velocity fluctuations in Fig. 15(a) and smaller anisotropy in Fig. 15(b).

In short, as the particle size d_p increases from fine to coarse particles, then the Stokes number St_p increases, resulting in greater particle inertia and higher wall constraint at a given pipe diameter. From the comparison of Figs. 15(a) and 17–19, it is not difficult to see that there are two flow regimes between smaller and larger St_p, that is, there are indeed significant differences between fine particles and coarse particles.

VI. CONCLUSION

In this paper, the semi-resolved CFD-DEM based on CFDEM is applied to explore particle mixing and segregation behaviors with different size ratios, then analyze the differences in particle dynamics between fine and coarse particles, and finally reveal the mechanics for the differences:

(i) First, the changes in particle mixing and segregation behaviors and the network of contact forces with different size ratios are analyzed. For a larger size ratio (2.5), the plug is obvious and the contact force network is stronger. For a smaller size ratio (1.43), the contact force network and the plug are weaker. Thus, the plug is likely to occur in larger size ratios. To ensure safety in engineering, the difference in particle size should not be too large in fluidized beds with different size ratios.

(ii) Second, after the segregation of species 1 and 2, the differences in particle dynamics of species 2 such as velocity fluctuations, autocorrelation time and length scales, and radial distribution functions are studied. For autocorrelation length scales, it is the obvious difference in the normalized autocorrelation length that is greater than 1 at smaller St_p (1.96, 4.42, and 7.86), but smaller than 1 at larger St_p (12.28, 17.68, and 24.06). In addition, the anisotropy decreases with the increase of St_p. For radial distributions, there are two peaks at $r/d_p = 1$ and $r/d_p = 2$, indicating that particles are likely to appear in the two positions, and two flow regimes are observed at $g(r/d_p = 2)$.

(iii) Finally, the hydrodynamic stress, collision stress, and collision frequency are used to investigate the mechanism of differences in the particle dynamics between fine and coarse particles. The hydrodynamic stress is larger than the collision stress at smaller St_p, which indicates that the influence of mean flow is more important in this case. However, the hydrodynamic stress is smaller than the collision stress at larger St_p, which evidences that the collisions are prominent at larger St_p. The collision frequency increases with the increase of St_p, which explains why the anisotropy decreases with the increase of St_p. Eventually, it is the main reason for the difference in particle dynamics between fine and coarse particles that the effects of collisions are greater than that of the hydrodynamic effects with the increase of St_p.

ACKNOWLEDGMENTS

This work was supported by the National Natural Science Foundation of China (Grant No. 12132018), the Strategic Priority

Research Program of the Chinese Academy of Sciences (Grant No. XDA22000000), and the Youth Innovation Promotion Association of Chinese Academy of Sciences (Grant No. 2017027).

AUTHOR DECLARATIONS

Conflict of Interest

The authors have no conflicts to disclose.

Author Contributions

Wanlong Ren: Data curation (equal); Investigation (equal); Methodology (equal); Validation (equal); Writing – original draft (lead); Writing – review & editing (equal). **Xuhui Zhang:** Conceptualization (equal); Funding acquisition (lead); Methodology (equal); Resources (equal); Supervision (equal); Writing – review & editing (equal). **Yan Zhang:** Conceptualization (equal); Data curation (equal); Investigation (equal); Methodology (equal); Software (equal); Supervision (equal); Writing – review & editing (equal). **Peng Li:** Data curation (equal); Methodology (equal); Software (equal); Validation (equal); Visualization (equal); Writing – review & editing (equal). **Xiaobing Lu:** Conceptualization (equal); Investigation (equal); Methodology (equal); Resources (equal); Software (equal); Writing – review & editing (equal).

DATA AVAILABILITY

The data that support the findings of this study are available from the corresponding author upon reasonable request.

REFERENCES

[1]Y. Yao, C. S. Criddle, and O. B. Fringer, "Competing flow and collision effects in a monodispersed liquid–solid fluidized bed at a moderate Archimedes number," J. Fluid Mech. **927**, A28 (2021).
[2]W. Chen, H.-L. Xu, F.-q. Yang, X. Rao, Y.-X. Zhou, D. Hu, and L. Peng, "Research on the transportation and flow characteristics of deep-sea ore transportation equipment," Appl. Ocean Res. **113**, 102765 (2021).
[3]J. Richardson and W. Zaki, "Sedimentation and fluidization: Part I," Chem. Eng. Res. Des. **75**, S82–S100 (1997).
[4]Z. Xie, S. Wang, and Y. Shen, "CFD-DEM study of segregation and mixing characteristics under a bi-disperse solid–liquid fluidised bed," Adv. Powder Technol. **32**, 4078–4095 (2021).
[5]N. Epstein and B. LeClair, "Liquid fluidization of binary particle mixtures. II. Bed inversion," Chem. Eng. Sci. **40**, 1517–1526 (1985).
[6]F. D. Cúñez and E. Franklin, "Plug regime in water fluidized beds in very narrow tubes," Powder Technol. **345**, 234–246 (2019).
[7]B. Pei, K. Zhao, Z. Luo, L. Zhao, and B. Bai, "Particle dispersion in turbulent mixing layer at supercritical pressure," Powder Technol. **412**, 118010 (2022).
[8]A. Di Renzo, F. Cello, and F. P. Di Maio, "Simulation of the layer inversion phenomenon in binary liquid–fluidized beds by DEM–CFD with a drag law for polydisperse systems," Chem. Eng. Sci. **66**, 2945–2958 (2011).
[9]L. Gibilaro, I. Hossain, and S. Waldram, "On the Kennedy and Bretton model for mixing and segregation in liquid fluidized beds," Chem. Eng. Sci. **40**, 2333–2338 (1985).
[10]H. Moritomi, T. Iwase, and T. Chiba, "A comprehensive interpretation of solid layer inversion in liquid fluidised beds," Chem. Eng. Sci. **37**, 1751–1757 (1982).
[11]R. Escudié, N. Epstein, J. R. Grace, and H. T. Bi, "Layer inversion phenomenon in binary-solid liquid-fluidized beds: Prediction of the inversion velocity," Chem. Eng. Sci. **61**, 6667–6690 (2006).
[12]F. P. Di Maio and A. Di Renzo, "Direct modeling of voidage at layer inversion in binary liquid-fluidized bed," Chem. Eng. J. **284**, 668–678 (2016).
[13]Z. Peng, E. Doroodchi, C. Luo, and B. Moghtaderi, "Influence of void fraction calculation on fidelity of CFD-DEM simulation of gas–solid bubbling fluidized beds," AIChE J. **60**, 2000–2018 (2014).
[14]W.-L. Ren, Y. Zhang, X.-H. Zhang, and X.-B. Lu, "Investigation of the characteristics and mechanisms of the layer inversion in binary liquid–solid fluidized beds with coarse particles," Phys. Fluids **34**, 103325 (2022).
[15]F. D. Cúñez and E. M. Franklin, "Crystallization and jamming in narrow fluidized beds," Phys. Fluids **32**, 083303 (2020).
[16]J. Van Wijk, A. Talmon, and C. van Rhee, "Stability of vertical hydraulic transport processes for deep ocean mining: An experimental study," Ocean Eng. **125**, 203–213 (2016).
[17]F. D. Cúñez and E. M. Franklin, "Mimicking layer inversion in solid-liquid fluidized beds in narrow tubes," Powder Technol. **364**, 994–1008 (2020).
[18]Z. Zhou and A. Yu, "Simulation of the flow and segregation of particle mixtures in liquid fluidization," AIP Conf. Proc. **1145**, 993–996 (2009).
[19]E. A. Molaei, A. Yu, and Z. Zhou, "Investigation of causes of layer inversion and prediction of inversion velocity in liquid fluidizations of binary particle mixtures," Powder Technol. **342**, 418–432 (2019).
[20]P. Duru and É. Guazzelli, "Experimental investigation on the secondary instability of liquid-fluidized beds and the formation of bubbles," J. Fluid Mech. **470**, 359–382 (2002).
[21]P. Duru, M. Nicolas, J. Hinch, and E. Guazzelli, "Constitutive laws in liquid-fluidized beds," J. Fluid Mech. **452**, 371–404 (2002).
[22]F. D. Cúñez, N. C. Lima, and E. M. Franklin, "Motion and clustering of bonded particles in narrow solid–liquid fluidized beds," Phys. Fluids **33**, 023303 (2021).
[23]Y. Zhang, X.-B. Lu, and X.-H. Zhang, "Numerical simulation on transportation behavior of dense coarse particles in vertical pipe with an optimized Eulerian–Lagrangian method," Phys. Fluids **34**, 033305 (2022).
[24]M. Zhou, S. Wang, S. Kuang, K. Luo, J. Fan, and A. Yu, "CFD-DEM modelling of hydraulic conveying of solid particles in a vertical pipe," Powder Technol. **354**, 893–905 (2019).
[25]C. Wan, S. Xiao, D. Zhou, H. Zhu, Y. Bao, K. Kakanda, and Z. Han, "Numerical simulation on transport behavior of gradated coarse particles in deep-sea vertical pipe transportation," Phys. Fluids **35**, 043328 (2023).
[26]Y. Dai, Y. Zhang, and X. Li, "Numerical and experimental investigations on pipeline internal solid–liquid mixed fluid for deep ocean mining," Ocean Eng. **220**, 108411 (2021).
[27]T. Lichtenegger and T. Miethlinger, "On the connection between Lagrangian and Eulerian metrics for recurrent particulate flows," Phys. Fluids **32**, 113308 (2020).
[28]H. Li, X. Ku, and J. Lin, "Eulerian–Lagrangian simulation of inertial migration of particles in circular Couette flow," Phys. Fluids **32**, 073308 (2020).
[29]W.-L. Ren, X.-H. Zhang, Y. Zhang, and X.-B. Lu, "Investigation of motion characteristics of coarse particles in hydraulic collection," Phys. Fluids **35**, 043322 (2023).
[30]Q. Dai, T. Jin, K. Luo, W. Xiao, and J. Fan, "Direct numerical simulation of a three-dimensional spatially evolving compressible mixing layer laden with particles. II. Turbulence anisotropy and growth rate," Phys. Fluids **31**, 083303 (2019).
[31]Z. Shen, G. Wang, D. Huang, and F. Jin, "A resolved CFD-DEM coupling model for modeling two-phase fluids interaction with irregularly shaped particles," J. Comput. Phys. **448**, 110695 (2022).
[32]J. Zeng, P. Tang, H. Li, and D. Zhang, "Simulating particle settling in inclined narrow channels with the unresolved CFD-DEM method," Phys. Rev. Fluids **6**, 034302 (2021).
[33]Y. Wang, K. Cheng, Y. Yang, Y. Tao, and Y. Li, "Microscopic mechanical analysis of sand production using a new arbitrary resolved-unresolved CFD-DEM model," Int. J. Multiphase Flow **149**, 103979 (2022).
[34]Y.-h. Sun, W.-t. Zhang, X.-l. Wang, and Q.-q. Liu, "Numerical study on immersed granular collapse in viscous regime by particle-scale simulation," Phys. Fluids **32**, 073313 (2020).
[35]K. Cheng, Y. Wang, and Q. Yang, "A semi-resolved CFD-DEM model for seepage-induced fine particle migration in gap-graded soils," Comput. Geotech. **100**, 30–51 (2018).
[36]B. Vowinckel, J. Withers, P. Luzzatto-Fegiz, and E. Meiburg, "Settling of cohesive sediment: Particle-resolved simulations," J. Fluid Mech. **858**, 5–44 (2019).

[37]Z. Wang, Y. Teng, and M. Liu, "A semi-resolved CFD–DEM approach for particulate flows with kernel based approximation and Hilbert curve based searching strategy," J. Comput. Phys. **384**, 151–169 (2019).
[38]Y. Zhang, X.-B. Lu, and X.-H. Zhang, "An optimized Eulerian–Lagrangian method for two-phase flow with coarse particles: Implementation in open-source field operation and manipulation, verification, and validation," Phys. Fluids **33**, 113307 (2021).
[39]C. Goniva, C. Kloss, N. G. Deen, J. A. Kuipers, and S. Pirker, "Influence of rolling friction on single spout fluidized bed simulation," Particuology **10**, 582–591 (2012).
[40]R. Berger, C. Kloss, A. Kohlmeyer, and S. Pirker, "Hybrid parallelization of the LIGGGHTS open-source DEM code," Powder Technol. **278**, 234–247 (2015).
[41]R. Zhao, Y. Zhou, D. Zhang, and X. Gao, "Numerical investigation of the hydraulic transport of coarse particles in a vertical pipe based on a fully-coupled numerical model," Int. J. Multiphase Flow **155**, 104094 (2022).
[42]P. A. Cundall and O. D. Strack, "A discrete numerical model for granular assemblies," Geotechnique **29**, 47–65 (1979).
[43]H. Zhu, Z. Y. Zhou, R. Yang, and A. Yu, "Discrete particle simulation of particulate systems: Theoretical developments," Chem. Eng. Sci. **62**, 3378–3396 (2007).
[44]L. Li, B. Li, and Z. Liu, "Modeling of spout-fluidized beds and investigation of drag closures using openFOAM," Powder Technol. **305**, 364–376 (2017).
[45]Z. Zhou, S. Kuang, K. Chu, and A. Yu, "Discrete particle simulation of particle–fluid flow: Model formulations and their applicability," J. Fluid Mech. **661**, 482–510 (2010).
[46]R. Di Felice, "The voidage function for fluid-particle interaction systems," Int. J. Multiphase Flow **20**, 153–159 (1994).
[47]E. Loth and A. J. Dorgan, "An equation of motion for particles of finite Reynolds number and size," Environ. Fluid Mech. **9**, 187–206 (2009).
[48]R. I. Issa, "Solution of the implicitly discretised fluid flow equations by operator-splitting," J. Comput. Phys. **62**, 40–65 (1986).
[49]G. Chen, H. Wang, K. Luo, and J. Fan, "Two-way coupled turbulent particle-laden boundary layer combustion over a flat plate," J. Fluid Mech. **948**, A12 (2022).
[50]J. Friedrich, B. Viggiano, M. Bourgoin, R. B. Cal, and L. Chevillard, "Single inertial particle statistics in turbulent flows from Lagrangian velocity models," Phys. Rev. Fluids **7**, 014303 (2022).
[51]L. Nicolaou and T. Zaki, "Characterization of aerosol stokes number in 90° bends and idealized extrathoracic airways," J. Aerosol Sci. **102**, 105–127 (2016).
[52]E. A. Schnorr Filho, N. C. Lima, and E. M. Franklin, "Resolved CFD-DEM simulations of the hydraulic conveying of coarse grains through a very-narrow elbow," Powder Technol. **395**, 811–821 (2022).
[53]Y. Tsuji, T. Kawaguchi, and T. Tanaka, "Discrete particle simulation of two-dimensional fluidized bed," Powder Technol. **77**, 79–87 (1993).
[54]S. Ergun and A. A. Orning, "Fluid flow through randomly packed columns and fluidized beds," Ind. Eng. Chem. **41**, 1179–1184 (1949).
[55]A. Esteghamatian, A. Hammouti, M. Lance, and A. Wachs, "Particle resolved simulations of liquid/solid and gas/solid fluidized beds," Phys. Fluids **29**, 033302 (2017).
[56]J. Fu, S. Chen, and X. Zhou, "Effect of heterogeneity on interphase heat transfer for gas–solid flow: A particle-resolved direct numerical simulation," Phys. Fluids **34**, 123317 (2022).
[57]D. P. Willen and A. Prosperetti, "Resolved simulations of sedimenting suspensions of spheres," Phys. Rev. Fluids **4**, 014304 (2019).
[58]X. Yin and D. L. Koch, "Lattice-Boltzmann simulation of finite Reynolds number buoyancy-driven bubbly flows in periodic and wall-bounded domains," Phys. Fluids **20**, 103304 (2008).
[59]J. Zhang, M.-J. Ni, and J. Magnaudet, "Three-dimensional dynamics of a pair of deformable bubbles rising initially in line. I. Moderately inertial regimes," J. Fluid Mech. **920**, A16 (2021).